Genetic load determines atrophy in hand cortico-striatal pathways in presymptomatic Huntington's disease

Yi Hong, Lauren J O 'Donnell, Peter Savadjiev, Fan Zhang, Demian Wassermann, Ofer Pasternak, Hans J Johnson, Jane Paulsen, Jean-Paul Vonsattel, Nikolaos Makris, et al.

Genetic load determines atrophy in hand cortico-striatal pathways in presymptomatic Huntington's disease

Yi Hong[1*], Lauren J. O'Donnell[2], Peter Savadjiev[2], Fan Zhang[2], Demian Wassermann[6], Ofer Pasternak[2], Hans Johnson[4], Jane Paulsen[4], Jean-Paul Vonsattel[5], Nikolaos Makris[3], Carl F. Westin[2†], and Yogesh Rathi[2†]

1 Department of Computer Science, University of Georgia, Athens, GA, USA

2 Department of Radiology, Brigham and Women's Hospital, Harvard Medical School, Boston, MA, USA

3 Department of Psychiatry, Massachusetts General Hospital, Harvard Medical School, Boston, MA, USA

4 Department of Psychiatry, University of Iowa, Iowa City, IA, USA

5 Department of Pathology and Cell Biology, Columbia University, New York, NY, USA

6 Athena team, INRIA Sophia Antipolis Mediterranee, France

* 415 Boyd Graduate Studies Research Center, University of Georgia, Athens, GA 30602

yi.hong@uga.edu, (706) 542-8214

† Equal contribution

Abstract

Huntington's disease (HD) is an inherited neurodegenerative disorder that causes progressive breakdown of striatal neurons. Standard white matter integrity measures like fractional anisotropy and mean diffusivity derived from diffusion tensor imaging were analyzed in prodromal-HD subjects; however, they studied either a whole brain or specific subcortical white matter structures with connections to cortical motor areas. In this work, we propose a novel analysis of a longitudinal cohort of 243 prodromal-HD individuals and 88 healthy controls who underwent two or more diffusion MRI scans as part of the PREDICT-HD study. We separately trace specific white matter fiber tracts connecting the striatum (caudate and putamen) with four cortical regions corresponding to the hand, face, trunk, and leg motor areas. A multi-tensor tractography algorithm with an isotropic volume fraction compartment allows

estimating diffusion of fast-moving extra-cellular water in regions containing crossing fibers and provides quantification of a microstructural property related to tissue atrophy. The tissue atrophy rate is separately analyzed in eight cortico-striatal pathways as a function of CAG-repeats (genetic load) by statistically regressing out age effect from our cohort. The results demonstrate a statistically significant increase in isotropic volume fraction (atrophy) bilaterally in hand fiber connections to the putamen with increasing CAG-repeats, which connects the genetic abnormality (CAG-repeats) to an imaging-based microstructural marker of tissue integrity in specific white matter pathways in HD. Isotropic volume fraction measures in eight cortico-striatal pathways are also correlated significantly with total motor scores and diagnostic confidence levels, providing evidence of their relevance to HD clinical presentation.

Keywords: Prodromal-HD, diffusion MRI, isotropic volume fraction, CAG-repeats, cortico-striatal pathways

1. Introduction

Huntington's disease (HD) is a genetic brain disorder that causes physical and mental decline, including uncontrollable movements, emotional problems, and loss of thinking abilities. Huntington's disease is caused by expansion of CAG (cytosine-adenine-guanine) repeats in the Huntington (HTT) gene, with a threshold of 36 or more repeats (Vonsattel and DiFiglia, 1998). During the presymptomatic (prodromal-HD) phase, individuals do not manifest the characteristic motor symptoms necessary for a diagnosis, but they have been shown to exhibit mild sub-clinical cognitive, psychiatric and motor deficits. Symptoms of Huntington's disease vary between individuals and its progression may evolve over years before formal diagnosis. Studies show that brain atrophy occurs gradually and typically starts years before symptom onset. Although this inherited disease currently has no cure, identification of reliable markers might be useful for future Huntington's disease clinical trials to monitor disease progression and evaluate therapeutic efficacy (Ross et al., 2014).

Neuroimaging provides a powerful tool for detecting, understanding, and monitoring disease progression. Early works proposed to use Magnetic Resonance Imaging (MRI) to elucidate structural abnormalities in Huntington's disease (Bohanna et al., 2008; Georgiou-Karistianis et al., 2013). In the PREDICT-HD and TRACK-HD studies, MRI measures, e.g., the whole-brain volume, caudate and putamen volumes, were examined to understand Huntington's disease progression (Paulsen et al., 2008; Tabrizi et al., 2013; Paulsen et al., 2014). Several studies

have shown that volume reductions in the striatum, particularly within the caudate, can be observed as early as 10 years before diagnosis in prodromal-HD individuals (Harris et al., 1999; Thieben et al., 2002; Paulsen et al., 2008). Volume reductions in the globus pallidus (Harris et al., 1999; Thieben et al., 2002) and thalamus (Harris et al., 1999; Paulsen et al., 2006) have also been observed. The literature on cortical thinning has however been controversial. While some studies have found decreased cortical thickness in prodromal-HD (Rosas et al., 2005; Nopoulos et al., 2007; Bohanna et al., 2008), others have found increased grey matter volume (Aylward et al., 1996; Alyward et al., 1998; Paulsen et al., 2006). The relatively large longitudinal TRACK-HD study failed to find differences in cortical volumes at baseline and 12 months (Tabrizi et al., 2009; Tabrizi et al., 2011) in prodromal-HD, but did find reduced cortical thickness in occipital areas in prodromal-HD individuals who were closest to diagnosis at 24 months (Tabrizi et al., 2012), suggesting that cortical thickness changes may not be tied to motor symptom onset or that they occur only as secondary collateral damage measurable late in the prodromal-HD stage of the illness.

In addition to volumetric measures, studies of tissue microstructure have shown changes in Huntington's disease. Mean diffusivity derived from diffusion weighted magnetic resonance imaging (dMRI) was found to have increased in the prefrontal cortex of prodromal-HD subjects (Rosas et al., 2006; Phillips et al., 2013; Matsui et al., 2014). In addition, the IMAGE-HD study (Poudel et al., 2015) showed evidence of longitudinal decline in white matter integrity in symptomatic Huntington's disease using diffusion tensor imaging (DTI, a special case of dMRI which assumes a Gaussian diffusion profile at each voxel) data. DTI studies have also provided evidence of white matter degeneration in terms of reduced fractional anisotropy and increased radial diffusivity. It was suggested that these measures may provide unique information about the time-course and diagnosis of neurodegeneration in prodromal-HD (Liu et al., 2016). Other studies have reported reduced fractional anisotropy in several regions including the corpus callosum (Stoffers et al., 2010; Phillips et al., 2013), frontal tracts (Poudel et al., 2014; Phillips et al., 2014), thalamic tracts (Stoffers et al., 2010; Phillips et al., 2014), and white matter surrounding the striatum (Stoffers et al., 2010). These DTI findings have been thought to reflect degeneration at the cellular level and a reduction in white matter tract integrity (due to reduction in fractional anisotropy). Another recent work (Shaffer et al., 2016) used a multi-tensor tractography framework to analyze changes in the motor pathways in three groups clustered using the CAP score (product of CAG-repeats and age). The results showed significant differences in fractional anisotropy in the three groups in the motor pathways.

However, as has been shown in several recent works in diseases such as schizophrenia and Parkinson's (Pasternak et al., 2015; Rotenberg et al., 2015; Planetta et al., 2016), the DTI model is simplistic and may not be appropriate to draw inferences about the neurobiological abnormalities in tissue. Adding an isotropic volume fraction compartment (Pasternak et al., 2009) to the standard DTI model provides more specificity and allows to quantify the volume fraction of fast moving extra-cellular water. The existence of the isotropic volume fraction has been validated in mouse models of demyelination and tissue loss (Wang et al., 2011). Similarly, it has been used in popular models like neurite orientation dispersion and density imaging (NODDI) (Zhang et al., 2012). In their work on comparing different diffusion models, Panagiotaki et al. show that adding an isotropic compartment better explains the dMRI signal (Panagiotaki et al., 2012).

In the study of schizophrenia and Parkinson's (Pasternak et al., 2015; Rotenberg et al., 2015; Planetta et al., 2016), the authors have shown that including this isotropic volume fraction compartment provides better neurobiological clarity about the underlying tissue abnormality. For example, an increase in the isotropic volume fraction component could indicate loss of neurons or tissue atrophy. In schizophrenia, a simple DTI model pointed to decreased fractional anisotropy in several brain regions implying decreased white matter integrity. However, incorporating the isotropic volume fraction model pointed to widespread neuro-inflammation as a possible mechanism and very little change in white matter integrity (Pasternak et al., 2009; Pasternak et al., 2015). Thus, we hypothesize that the inferences drawn from the DTI model about reduced white matter integrity in Huntington's disease may not be entirely accurate and need to be further tested using more advanced models of diffusion as is done in this work.

Recent studies on mouse models of Huntington's disease have reported the existence of widespread brain atrophy in several brain regions (Steventon et al., 2016). Consequently, in this paper, we propose to use the isotropic volume fraction (a measure of tissue atrophy) estimated in an unscented Kalman filter based multi-tensor tractography framework (Malcolm et al., 2010; Baumgartner et al., 2012) to characterize white matter atrophy in prodromal-HD subjects. This framework allows to trace fiber tracts through crossing fiber regions while simultaneously estimating the isotropic volume fraction along the tracts. We hypothesize that we see a higher isotropic volume fraction in prodromal-HD subjects compared to normal controls, indicating increased brain atrophy. Note that, most earlier works have not investigated this aspect of Huntington's disease pathophysiology due to the limitations of the DTI model.

Another novel aspect of our work is the design of a methodology to extract specific cortico-striatal tracts corresponding to the hand, face, trunk, and leg motor regions, as shown in **Fig. 1**. Previous studies have shown that the cortico-striatal pathway in the brain is key to early Huntington's disease symptomatology and that Huntington's disease affects the white matter causing dysfunction due to neuronal loss in the striatal circuits and cortical neurons that make up the cortico-striatal pathways (Macdonal et al., 2002; Cepeda et al., 2003; Cepeda et al., 2007; Vonsattel et al., 2008). However, for the first time in this study, we trace and differentially analyze these specific tracts connecting the hand, face, trunk, and leg areas in the cortex to the caudate and putamen (Haber and Calzavara 2009) and estimate the isotropic volume fraction in these tracts in a large longitudinal data set. This allows us to evaluate the sensitivity of isotropic volume fraction to detect tissue atrophy in different motor areas and its specificity to different anatomical parts of the cortico-striatal pathway.

To investigate if specific cortico-striatal pathways exhibit differential rates of atrophy in prodromal-HD subjects, we analyze the PREDICT-HD data, which is a longitudinal dataset collected from gene expansion negative controls and subjects with prodromal-HD. Specifically, we investigate the longitudinal isotropic volume fraction from three perspectives: 1) its sensitivity to brain atrophy in prodromal-HD subjects in comparison to healthy controls; 2) its correlation to genetic load, the CAG repeats; 3) its correlation to behavioral and clinical tests, such as total motor scores and diagnostic confidence level. We performed these tests using linear mixed-effects models for the population of healthy controls and prodromal-HD, respectively. The experimental results (after multiple hypothesis correction) indicate that the isotropic volume fraction, specifically in the bilateral hand motor tracts could be used as an imaging marker of genetic load and symptom severity in prodromal-HD.

2. Materials and methods

In this work, we analyzed the longitudinal diffusion MRI data set of prodromal-HD subjects acquired as part of the PREDICT-HD project (Paulsen et al., 2014). Under the guidance of an expert neuroanatomist (Dr. Makris) we manually created a modification of the Desikan-Killiany cortical atlas (Desikan et al., 2006) typically used with FreeSurfer (Fischl et al., 2004), to produce a new atlas that includes delineations of the hand, face, trunk, and leg sub-regions of the motor cortex. These new expert-defined atlas regions were spatially mapped to the T1-weighted image of each individual subject. Whole brain multi-tensor tractography was performed on the dMRI data and white matter tracts connecting the striatum (caudate and putamen) with each of the four cortical motor regions were

extracted, as shown in **Fig. 1**. The isotropic volume fraction was estimated in each of the fiber bundles (a total of sixteen fiber bundles; four cortico-caudal and four cortico-putamen in each hemisphere) and mixed-effects models (Pinherio and Bates, 2004) were used to analyze the data as described in the subsequent section.

2.1. Linear mixed-effects model

Typically, regression models are selected to estimate the correlation between variables, for example, the correlation of the isotropic volume fraction with age, CAG, or total motor scores. Mixed-effects models are an extension of standard regression models and are more suitable for longitudinal data because they can account for the dependency due to repeated measures or data in groups. A mixed-effects model has both fixed and random effects while a standard regression model has only fixed effects. Specifically, the fixed-effects terms in a mixed-effects model correspond to the conventional regression part, and the random-effects terms are associated with individual experimental units drawn at random from a population. In this paper, we use a linear mixed-effects model to study a population of longitudinal data, i.e., the population of healthy controls and the population of prodromal-HD subjects. Assume in a population there are *N* subjects and the dMRI measures for subject i ($i = 1, \dots, N$) are collected at n_i time points. For such longitudinal data, the mixed-effects model estimates the relationship between a dMRI measure and associated subject attributes through multilevel regression. The model can be expressed as:

$$y_{ij} = \underbrace{\beta_0 + \beta_1 x_{ij}}_{\textit{fixed effects}} + \underbrace{\gamma_{0i} + \gamma_{1i} u_{ij}}_{\textit{random effects}} + \epsilon_{ij}, \quad i = 1, 2, \dots, N, \quad j = 1, 2, \dots, n_i. \tag{1}$$

Here, y_{ij} corresponds to the response, e.g., the isotropic volume fraction, for the i-th individual measured at the j-th time point; x_{ij} is the independent variable and depends on the task, e.g., the age of the subject or the CAG repeats if we regress out the age effect later; u_{ij} is the independent variable in the random effect term analogous to x_{ij}. The parameters β_0 and β_1 are the average intercept and slope shared among the population, while γ_{0i} and γ_{1i} are the random effects intercept and slope, the specific parameters for subject i. The random variable $\epsilon_{ij} \sim N(0, \sigma^2)$ is the independent error, which follows a normal distribution with zero mean and a standard deviation of σ. The random effects are designed to account for the dependency of the data in several variables. For example, the dependency could exist in the data collected from the same subject, the same gender (Zielonka et al. 2013), the same scanner, or subjects with the same CAG repeats. Hence, our linear mixed-effects model has the following formulation:

$$y_{ij} = \underbrace{\beta_0 + \beta_1 x_{ij}}_{\textit{fixed effects}} + \underbrace{\gamma_{0i}^{sub} + \gamma_{1i}^{sub} u_{ij}}_{\substack{\textit{random effects} \\ \textit{subject-specific}}} + \underbrace{\gamma_{0k}^{gen} + \gamma_{1k}^{gen} v_{ij}}_{\substack{\textit{random effects} \\ \textit{gender-specific}}} + \underbrace{\gamma_{0r}^{CAG} + \gamma_{1r}^{CAG} w_{ij}}_{\substack{\textit{random effects} \\ \textit{CAG-specific}}} + \underbrace{\gamma_{0s}^{scan} + \gamma_{1s}^{scan} s_{ij}}_{\substack{\textit{random effects} \\ \textit{scanner-specific}}} + \epsilon_{ij}, \tag{2}$$

where k represents male or female, r is the number of CAG repeats, s represents the scanner site; while u_{ij}, v_{ij}, w_{ij}, and s_{ij} are random effect variables analogous to x_{ij}. Note that our data was collected at several different sites, and hence we use the scanner site as a co-variate to account for scanner related differences. This linear mixed-effects model can be used to detect the caudate and putamen volume loss over age, to measure the change in the isotropic volume fraction with age in a population, and to estimate the correlation of the isotropic volume fraction with total motor scores and diagnostic confidence levels.

Meanwhile, we are also interested in exploring the correlation between the isotropic volume fraction and CAG repeats for Huntington's disease subjects. As is known from literature, dMRI measures such as fractional anisotropy and the isotropic volume fraction change with age. To compute correlation between the isotropic volume fraction and CAG repeats, we should first remove the effect of age on the estimated the isotropic volume fraction. Therefore, we estimated the change in the isotropic volume fraction with age in the normal control population and regressed it out from the HD group. In particular, we used the above linear mixed-effects model (Eq. 2) to estimate the normal control group trend, represented by the fixed effects parameters (β_0^{normal} and β_1^{normal}). With respect to the estimated normal control group trend, we compute the residuals of the isotropic volume fraction for prodromal-HD subjects δy_{ij}^{HD} as follows:

$$\delta y_{ij}^{HD} = y_{ij}^{HD} - (\beta_0^{normal} + \beta_1^{normal} x_{ij}^{HD}), \quad (3)$$

where x_{ij}^{HD} represents the age of the HD subject and y_{ij}^{HD} represents its measured the isotropic volume fraction. This is further used to compute the correlations between the residuals and CAG repeats using the linear mixed-effects model. In this task, since the age effect has been regressed out, x_{ij} in Eq. 2 corresponds to CAG repeats, y_{ij} corresponds to the isotropic volume fraction residuals for prodromal-HD subjects, and the random effects involve the subject-, gender-, and scanner-specific dependency.

2.2. PREDICT-HD data

We use data collected by the PREDICT-HD project (Paulsen et al., 2014), an observational study of the earliest signs of Huntington's disease. This study involved more than 600 participants, but we used the data from only those individuals who have at least two MRI scans. This yielded 331 subjects with 830 scans collected at 2 to 5 time

191 points. Specifically, 202 subjects have 2 scans, 94 subjects have 3 scans, 31 subjects have 4 scans, and 4 subjects
192 have 5 scans. Additionally, the PREDICT-HD study provides genetic load for each subject, i.e., the CAG repeats,
193 and clinical scores, e.g., total motor scores and diagnostic confidence levels after each visit. The demographic and
194 clinical information of the data used in this study is shown in **Table 1**.
195 **Participants.** This study included 243 individuals with prodromal-HD and 88 normal controls. All participants were
196 right handed and underwent at least two longitudinal imaging sessions, resulting in a total of 611 prodromal-HD and
197 219 healthy control imaging sessions. Additional demographic characteristics for this sample are shown in **Table 1**.
198 The groups did not differ in terms of number of imaging sessions performed per participant, overall duration of time
199 between imaging sessions, or education. PREDICT-HD exclusion criteria included (a) sufficient motor signs for a
200 motor diagnosis at study entry; (b) history of traumatic brain injury or other central nervous system injury or
201 diseases; (c) pacemakers or metallic implants; (d) prescribed antipsychotic or phenothiazine-derivative antiemetic
202 medication in the past six months; and (e) clinical evidence of unstable medical or psychiatric illness.
203
204 **Imaging Parameters.** A total of 830 T1 and T2-weighted anatomical and diffusion-weighted images were acquired
205 on 3T scanners at 15 sites, representing 3 scanner manufacturers (GE, Phillips, and Siemens). Due to varying
206 scanning site capabilities and support resources, a minimum set of criteria were specified for merging the diffusion-
207 weighted imaging (DWI) data sets from different sites: 1) Only DWI data sets with more than 28 quality approved
208 gradient directions, 2) voxel volume was required to be less than 9.6 cubic mm with a maximum voxel length of
209 2.4mm, 3) All directional gradients needed to be within 2% of 1000 for their b-value, and 4) anatomical coverage
210 needed to completely include all the tracts of interest. The most frequently used MRI acquisition parameters are
211 given in **Table 2**. After visual inspection of all images, we excluded 13 T2-weighted MRI scans, resulting in 636
212 multimodal and 13 single modal inputs for structural MRI processing. Processed T2-weighted images were then
213 used along with DWI data in the diffusion analysis pipeline and the T1-weighted images were used for the 13
214 sessions where the T2- weighted images were not available.
215
216 ## 2.3. Image Processing
217 Structural and diffusion-weighted MR images were processed using the BRAINSTools suite
218 (https://github.com/BRAINSia/ BRAINSTools.git) and ANTs packages (Avants et al., 2009). An extensible

processing pipeline was developed in Nipype (Gorgolewski et al., 2011) that utilizes high performance computing resources to achieve time-efficient data processing and tractography analysis on large-scale multi-center diffusion-weighted images.

Structural MRI Processing. Structural MR Images (T2-weighted (T2-w) and/or T1-weighted (T1-w) images) were utilized to fix susceptibility-induced anatomical distortions in diffusion-weighted imaging data and provide precise anatomical labeling for dMRI processing and analysis. All available structural modalities, T1- and when available T2-weighted images, of each dataset were processed jointly to improve the robustness of the processing using complimentary information provided by multiple modalities. In the 13 cases where the T2 image was not available, a T1-only data processing was performed to identify anatomical brain regions. The T1-only morphometric processing was accurate enough for the subsequent tracts of interest extraction method. First, structural MR data were spatially normalized to a common reference orientation defined by anterior commissure-posterior commissure (AC-PC) line and inter-hemispheric fissure (Lu and Johnson, 2010; Ghayoor et al., 2017). The images were then processed through an Expectation Maximization (EM) and a fuzzy k-Nearest Neighbor (KNN) tissue classification that incorporates bias-field correction, image registration, and tissue classification (Kim and Johnson, 2013; Ghayoor et al., 2016). Whole brain segmentation (i.e. labeling) was performed first by applying the standard FreeSurfer pipeline (Fischl et al., 2004), and then by augmenting the resulting Desikan-Killany segmenation of the cortex (Desikan et al., 2006) with a custom-made parcellation of the motor cortex into four functional sub-regions, as described in further detail in a section below.

Diffusion MRI Processing. The dMRI processing first employed the quality-control procedures described in our previous works (Matsui et al., 2014; Oguz et al., 2014) to prepare dMRI scans by removing slice-wise and interlace artifacts as well as correcting for eddy-current and motion artifacts. The quality-controlled dMRI scans were further processed to integrate susceptibility artifact correction using a non-linear constrained registration in the phase-encoding direction available from the ANTs packages (Avants et al., 2009). The constrained registration only allows warping within the plane (i.e. within image slice) for the phase encoding direction, and is primarily used to improve anatomical alignment of the diffusion images to the morphometric scans. To enhance the quality of our data and to allow for detection of multiple fibers from the sparse set of gradient directions acquired, we used our compressed

246 sensing algorithm (Michailovich et al., 2011; Rathi et al., 2014) to reconstruct the signal into a canonical set of 81
247 gradient orientations.

248 **Multi-tensor tractography.** Whole brain tractography was performed using our multi-fiber (multi-tensor) model to
249 trace through crossing fiber regions. The multi-tensor unscented Kalman filter tractography (UKFt) method
250 consisted of two anisotropic tensors along with an isotropic volume compartment to model fast extracellular water
251 diffusion (Malcolm et al., 2010; Baumgartner et al., 2012; Reddy and Rathi, 2016). The model estimated a convex
252 combination of weights for the anisotropic fiber compartment and the isotropic volume compartment with the
253 diffusivity of the isotropic volume set to 3×10^{-3} s/mm^2 as in our previous work (Pasternak et al., 2009;
254 Baumgartner et al., 2012). UKFt parameter settings were determined via empirical testing on a subset of the dataset.
255 To maximize sensitivity to the cortico-striatal connections, the fractional anisotropy and generalized anisotropy
256 thresholds for seeding/stopping tractography were set to 0.06, and 10 fiber seeds were initiated per voxel. All
257 tractography results (for all subjects) underwent a quality check using the white matter analysis (O'Donnell and
258 Westin, 2007) quality control tool, which enables rapid visual inspections of tractography results by human experts.
259 Subjects that failed this quality control check were excluded.

260 **Extracting cortico-striatal tracts for hand, face, trunk, and leg regions.** The extraction of the tracts under
261 investigation in the present study requires a cortical atlas that defines the hand, leg, face and trunk functional sub-
262 regions of the motor cortex. However, the standard Desikan-Killany atlas (Desikan et al., 2006) typically used with
263 FreeSurfer does not distinguish between different sub-regions of the motor cortex. However, the FreeSurfer
264 processing pipeline allows users to create custom-made cortical atlases (Fischl et al., 2004).

265 To that effect, under the guidance of an expert neuroanatomist (Dr. Makris), we manually delineated the hand, leg,
266 face and trunk sub-regions of the motor cortex on the anatomical (T1) MRI images of six healthy control subjects
267 that were not part of the present study. We then used the "mris_ca_train" FreeSurfer command to create a new atlas
268 which augments the standard Desikan-Killany atlas with these new four regions. Then, the "mris_ca_label" and
269 "mri_aparc2aseg" FreeSurfer commands were used to individually map this new atlas to all the subjects used in the
270 present study.

271 This newly created, custom-made cortical parcellation was used in conjunction with the White Matter Query
272 Language (WMQL) (Wassermann et al., 2016), in order to perform tract extraction. WMQL is a powerful,
273 automated tract extraction method that uses gray matter regions of interest from the cortical parcellation as

anatomical queries for constructing white matter tracts. Specifically, for each cerebral hemisphere in each subject, we used WMQL to extract the tracts that connect each of the four motor cortex subregions (hand, face, trunk, and leg) to one of the two subcortical nuclei (caudate, putamen), for a total of eight tracts for each hemisphere.

3. Results

Caudate/Putamen volume loss. To confirm the reported decrease in volume size of caudate and putamen (Paulsen et al., 2008) in our data set, we investigated the volume size changes in both normal control and prodromal-HD groups. The changes were captured by using a linear mixed-effects model as in Equation (2), where the explanatory variable is the age and the response variable is the volume size). By applying this model to the longitudinal data for the caudate and putamen, we estimated a global intercept β_0 and slope β_1 for each structure in each group. A p-value for each parameter was also obtained and adjusted by the use of linear step-up (LSU) procedure originally introduced by Benjamini and Hochberg (Benjamini and Hochberg, 1995) to indicate the significance of the estimate. As shown in **Fig. 2**, the solid lines depict the global trend of volume loss over age, and the bars depict the FDR-adjusted p-values of the global estimate of the slope. The adjusted p-values for the intercept estimates are all close to zero, which are not shown in **Fig. 2**. Considering a significance level of 0.05, all estimates for global intercepts and slopes are statistically significant (see **Supplementary material, Table 1** for the actual p-values). That is, there is a correlation between volume size of caudate and putamen with age. Compared with the normal control group, the prodromal-HD group had a reduced volume size for the caudate and the putamen and a significantly faster degeneration rate as expected.

Isotropic volume fraction changes over age for different sensorimotor areas. To investigate longitudinal changes in the isotropic volume fraction (related to tissue atrophy), we leverage the longitudinal data and use the linear mixed-effects model to estimate group trends for both normal controls and prodromal-HD groups. **Fig. 3** shows the isotropic volume fraction changes in fiber bundles from hand, face, trunk, and leg sensorimotor areas to left and right caudate and putamen, respectively. Overall, most of the estimated trends suggest an increase in the isotropic volume fraction with age, from the four cortical areas to the caudate and putamen. Based on the estimated p-values (after FDR correction) for the intercept (not shown in **Fig. 3**) and slope, the prodromal-HD group trends are all significant at the level of 0.05 (also see **Supplementary material, Table 2** for the actual p-values). For the

normal control group, while fiber bundles associated with the caudate have no significant increase in the isotropic volume fraction, some fiber bundles associated with the putamen show significant changes in the isotropic volume fraction, including the left putamen to hand, face, and leg areas, as well as the right putamen to hand, trunk, and leg regions (see **Fig. 3**). These results indicate that for Huntington's disease, significant isotropic volume fraction changes were detected in all cortico-striatal pathways, while for healthy controls the pathways connecting the putamen show more significant isotropic volume fraction changes than those connected to the caudate.

It is worth to mention that the isotropic volume faction contributes only about 10-15% (0.1-0.15) of the total signal volume fraction, as shown in Fig.3. This is small and in-line with that expected in white matter tissue. However, it is elevated in HD due to tissue atrophy. In light of the histology work of (Wang et al. 2011), it is likely that there exist small pockets of fast moving water within the tissue, which indicate tissue atrophy as is known to exist in HD.

Differential rate of increase in the isotropic volume fraction with age. To further investigate which region shows a faster rate of increase in the isotropic volume fraction (or atrophy), we estimated group trends in different regions for both normal control and prodromal-HD subjects. In particular, we compared the isotropic volume fraction difference between these two groups at age 50 (years), as the fit from linear regression has the lowest uncertainty at this age. Specifically, we estimated the isotropic volume fraction at age 50 for both groups and then computed their difference. To ensure robustness of the results, we color coded the rates such that the blue bars indicate connections for which the slope was statistically significant (after FDR correction). As shown in **Fig. 4** (top row), at the age of 50 years, the average isotropic volume fraction in the prodromal-HD group is larger than that for the normal control group in almost all cortico-striatal pathways. The top two significant fiber connections on the list are hand to the bilateral putamen, as shown on the top right of **Fig.4**.

In addition, the rate of increase in the isotropic volume fraction in prodromal-HD subjects is also faster than controls in almost all pathways. By discarding estimates with adjusted p-value larger than 0.05 (the gray bars in **Fig. 4**), the fiber bundles connecting hand and leg to right putamen show the fastest increase in the isotropic volume fraction (i.e., fastest rate of atrophy). The fiber bundle connecting hand to left putamen also shows similar rate of atrophy. **Thus, after accounting for the normal degeneration rate (from healthy controls), the cortico-striatal hand motor fibers seem to degenerate faster than other fiber tracts in Huntington's disease**.

Isotropic volume fraction correlation with genetic load. The number of CAG repeats determines whether a subject will develop Huntington's disease during his or her lifetime. We aim to find the correlation between this genetic load and isotropic volume fraction in the prodromal-HD group. To achieve this goal, we first regress out the effects of normal aging on changes in the isotropic volume fraction, and then estimate the relationship between the isotropic volume residuals and CAG repeats in prodromal-HD subjects. Although no significant correlations are found in caudal connections, motor regions connected to the putamen show significant correlations, for example, hand to the left and right putamen and leg to the right putamen, as shown in **Fig. 5** (also see **Supplementary material, Table 3** for the actual p-values). In addition, face to the left putamen and trunk to the right putamen (in **Fig. 5**) also show a significant change in the slope, indicating strong correlation between the isotropic volume fraction and CAG repeats in these regions. These results indicate that the isotropic volume fraction correlates with the genetic load in prodromal-HD subjects, and it further confirms that the putamen (and its motor connections) could play a critical role in early assessment of degeneration in Huntington's disease.

Isotropic volume fraction correlates with clinical scores. To further explore the relationship of the isotropic volume fraction with clinical scores, we used total motor scores and diagnostic confidence levels of prodromal-HD subjects using linear mixed-effects models. These scores are used to define motor diagnosis in at-risk individuals, and we study them only in prodromal-HD subjects. In addition, for each motor area we average the isotropic volume fraction from the bilateral tracts of the caudate or the putamen. The experimental results are shown in **Fig. 6**. In all regions except for trunk to the caudate for testing total motor scores correlation, the isotropic volume fraction was significantly correlated with both total motor scores and diagnostic confidence level with $p < 0.05$ (see FDR corrected p-values in **Supplementary material, Table 4**).

Exploratory tissue fractional anisotropy (FA_t) and mean diffusivity analyses. We also investigated if white matter integrity as measured by tract-specific fractional anisotropy (FA_t) was affected in prodromal-HD, as has been reported in several works using the standard DTI model (Poudel et al., 2015; Liu et al., 2016). Using our multi-tensor and isotropic volume compartment model, we found no statistically significant differences in the rate of change of FA_t (slope) with age between the prodromal-HD and normal control group. We note that the FA_t measure used in this work is obtained from the principal diffusion tensor estimated and oriented along the fiber tracts and thus is different than the standard DTI-based fractional anisotrophy measure (which does not account for crossing fibers). Further, FA_t also did not correlate with CAG-repeats in the prodromal-HD subjects. The change in mean

diffusivity (proportional to the trace of the principal diffusion tensor) with age also did not differ between the two groups, except for the fiber bundle connecting the putamen with the hand motor areas. Thus, when using a different model of diffusion, we find that only the atrophy-related measure of the isotropic volume fraction to be statistically different between the groups.

4. Discussion

In this paper, we present a unique longitudinal study of Huntington's disease in a large cohort of subjects by delineating specific fiber tracts connecting the striatum with four cortical motor regions, i.e., hand, face, trunk, and leg. Our approach utilizes the dependency in the longitudinal data by using linear mixed-effects models. We analyzed the isotropic volume fraction, a measure of tissue atrophy, in the cortico-striatal pathways and determined its correlation with age, genetic load, and clinical severity scores.

Previous studies on Huntington's disease often performed group comparison between Huntington's disease (or prodromal-HD) subjects and normal controls based on CAP scores (Zhang et al., 2011; Shaffer et al., 2016). The CAP score is computed using the number of CAG repeats and the subject's age. Here, instead of using the CAP score, we demonstrate a direct correlation of the isotropic volume fraction with CAG-repeats, by removing aging related effects in our longitudinal data. To the best of our knowledge, this is the first time that the genetic load in the prodromal-HD group has been shown to correlate with abnormality in specific cortico-striatal white matter tracts using an image-based marker. Significant correlations of the isotropic volume fraction (indicating atrophy) with CAG repeats are seen in connections to the four motor areas, especially to the hand motor areas (**Fig. 5**). The fibers connecting the cortical hand motor area demonstrate more atrophy than other motor areas. While our study connects the imaging, genetic and behavioral measures (motor scores), a recent study (Collins et al., 2014) showed that hand tapping performance was correlated with CAG-repeats and could be used as a longitudinal behavioral marker to assess progression of Huntington's disease. In a similar spirit, we believe that the proposed isotropic volume fraction estimated in the white matter tracts connecting the hand motor area could be used as an imaging marker of disease severity with possible use to monitor therapeutic interventions.

Furthermore, our results confirm earlier results on the volumetric loss in both caudate and putamen (Niccolini and Politis, 2014). A faster volume loss rate is detected in the caudate in prodromal-HD, as shown in **Fig. 2**. This result is consistent with the previous studies on longitudinal change in basal ganglia volume and studies on rate of caudate

atrophy in patients with Huntington's disease (Aylward et al., 1997; Aylward et al., 2000). This previous study suggested that change in caudate volume may be useful for assessing treatment effectiveness in both pre-symptomatic and symptomatic subjects. However, our analysis of white matter microstructure from dMRI measures in the cortico-striatal pathways shows that the fibers connecting motor areas to the putamen are more affected in prodromal-HD than those to the caudate, especially as demonstrated by the isotropic volume fraction changes over age (**Fig. 3**) and the correlation of the isotropic volume residuals with CAG-repeats (**Fig. 5**). A recent study (Singhal et al., 2017) also shows that caudate has a less degree of involvement in Huntington's disease and putaminal hypometabolism exceeds caudate changes on 18F-FDG PET imaging. Thus, the motor fibers connected to the putamen may be a better imaging marker for assessing structural changes in prodromal-HD.

Previous DTI studies on Huntington's disease suggested that fractional anisotropy is more sensitive than mean diffusivity in detecting structural changes in prodromal-HD (Liu et al., 2016). However, in our experiments, the isotropic volume fraction outperforms both fractional anisotropy and mean diffusivity by demonstrating stronger correlation with age and CAG-repeats. We should note that, using a more advanced model of diffusion that incorporates multiple crossing fibers and an isotropic volume compartment lends increased specificity and sensitivity to the obtained results as seen in studies on other neurodegenerative disorders such as Parkinson's disease (Planetta et al., 2016; Lyall et al., 2017). Our results indicate that the isotropic volume fraction could be a potential imaging maker for monitoring the progression of Huntington's disease.

Figure legend list:

Fig 1. White matter tracts connecting the striatum (top: caudate and bottom: putamen) with four cortical motor regions (left to right: hand, face, trunk, and leg).

Fig 2. Volume loss of the caudate and putamen over age. Lines illustrate estimates of the group trend for each population, normal controls (NC) or subjects with Huntington's disease (prodromal-HD). Grey areas show the 95% confidence intervals for the estimated group trends. Bars indicate the FDR-corrected p-values for the estimation of slope (decay rate).

Fig 3. Longitudinal analysis of the isotropic volume fraction of the caudate and putamen, connected with four motor regions, i.e., hand, face, trunk, and leg. Lines show the estimated group trend for each population, normal control

(NC) and prodromal-HD. Grey areas show the 95% confidence intervals for the estimated group trends. Bars present the FDR-adjusted p-values for the estimation of slope using the linear mixed-effects model. An adjusted p-value less than 0.05 indicates the estimate is significant and reliable. The title of each sub-figure details tractography connections that were reliably traced from the total scans in each group.

Fig 4. Comparison of the isotropic volume fraction between Normal Control (NC) and prodromal-HD groups. Top: the averaged isotropic volume fraction values estimated at the age of 50 years old for different regions. Bottom: the degeneration rates (slopes of estimated group trends) for different regions. From left to right: NC group, HD group, and their differences. Gray bars were used in those regions where estimate for the slope is not significant at the level of 0.05 (i.e., no significant correlation between isotropic volume fraction and age), while blue bars indicate that the results are significant at the level of 0.05. (Cau: Caudate, Put: Putamen).

Fig 5. Correlations between the isotropic volume fraction residuals (after regressing out the effect of age) and CAG repeats in prodromal-HD group for white matter connections to left caudate, left putamen, right caudate, and right putamen (from top to bottom). Lines depict estimates of group trends, gray areas indicate their 95% confidence intervals, and bars indicate the corresponding p-values of the estimated intercepts (β_0) and slopes (β_1). The title of each sub-figure details tractography connections and the number of scans for which robust connections were obtained out of total scans in prodromal-HD group.

Fig 6. Correlations between the isotropic volume fraction and (a) total motor scores (TMS), (b) diagnostic confidence level (DCL) in prodromal-HD group for caudate (top) and putamen (bottom). Lines show estimates of group trends, gray areas indicate their 95% confidence intervals, and bars present the corresponding FDR-corrected p-values of the estimated intercepts (β_0) and slopes (β_1).

Funding

This work was supported by U01NS083223 (PI: Westin), U01CA199459 (PI: O'Donnell Open Source Diffusion MRI Technology for Brain Cancer Research), R01MH097979 (PI: Rathi), P41EB015902 PI: Westin (co-investigators O'Donnell and Rathi), and Neuroimage Analysis Center.

References

Avants BB, Tustison NJ, Song G, Gee JC (2009): Ants: Open-source tools for normalization and neuroanatomy. HeanetIe 10: 1-11.

Aylward EH, Anderson NB, Bylsma FW, Wagster MV, Barta PE, Sherr M, et al. (1998): Frontal lobe volume in patients with Huntington's disease. Neurology 50(1): 252-258.

Aylward EH, Codori AM, Barta PE, Pearlson GD, Harris GJ, Brandt J (1996): Basal ganglia volume and proximity to onset in presymptomatic Huntington disease. Archives of neurology 53(12): 1293-1296.

Aylward EH, Codori AM, Rosenblatt A, Sherr M, Brandt J, Stine OC, et al. (2000): Rate of caudate atrophy in presymptomatic and symptomatic stages of Huntington's disease. Movement Disorders 15(3): 552-560.

Aylward EH, Li Q, Stine OC, Ranen N, Sherr M, Barta PE, et al. (1997): Longitudinal change in basal ganglia volume in patients with Huntington's disease. Neurology 48(2): 394-399.

Baumgartner C, Pasternak O, Bouix S, Westin CF, Rathi Y (2012): Filtered multi-tensor tractography using free water estimation. In International Society for Magnetic Resonance in Medicine Meeting.

Benjamini Y, Hochberg Y (1995): Controlling the false discovery rate: a practical and powerful approach to multiple testing. Journal of the royal statistical society Series B (Methodological): 289-300.

Bohanna I, Georgiou-Karistianis N, Hannan AJ, Egan GF (2008): Magnetic resonance imaging as an approach towards identifying neuropathological biomarkers for Huntington's disease. Brain research reviews 58: 209-225.

Cepeda C, Hurst RS, Calvert CR, Hernández-Echeagaray E, Nguyen OK, Jocoy E, et al. (2003): Transient and progressive electrophysiological alterations in the corticostriatal pathway in a mouse model of Huntington's disease. Journal of Neuroscience 23(3): 961-969.

461 Cepeda C, Wu N, André VM, Cummings DM, Levine MS (2007): The corticostriatal pathway in Huntington's
462 disease. Progress in neurobiology 81(5): 253-271.

463 Collins LM, Lazic SE, Barker RA (2014): A retrospective analysis of hand tapping as a longitudinal marker of
464 disease progression in Huntington's disease. BMC neurology 14(1): 1.

465 Desikan RS, Segonne F, Fischl B, Quinn BT, Dickerson BC, Blacker D, et al. (2006): An automated labeling system
466 for subdividing the human cerebral cortex on MRI scans into gyral based regions of interest. NeuroImage 31: 968–
467 980.

468 Fischl B, Van Der Kouwe A, Destrieux C, Halgren E, Ségonne F, Salat DH, et al. (2004): Automatically parcellating
469 the human cerebral cortex. Cerebral cortex 14(1): 11-22.

470 Georgiou-Karistianis N, Scahill R, Tabrizi SJ, Squitieri F, Aylward E (2013): Structural MRI in Huntington's
471 disease and recommendations for its potential use in clinical trials. Neuroscience and Biobehavioral Reviews 37:
472 480-490.

473 Ghayoor A, Paulsen JS, Kim RE, Johnson HJ (2016): Tissue classification of large-scale multi-site MR data using
474 fuzzy k-nearest neighbor method. In SPIE Medical Imaging International Society for Optics and Photonics: 97841V.

475 Ghayoor A, Vaidya JG, Johnson HJ (2017): Robust Automated Constellation-Based Landmark Detection in Human
476 Brain Imaging. Neuroimage.

477 Gorgolewski K, Burns CD, Madison C, Clark D, Halchenko YO, Waskom ML, et al. (2011): Nipype: a flexible,
478 lightweight and extensible neuroimaging data processing framework in python. Frontiers in neuroinformatics 5: 13.

479 Haber SN, Calzavara R (2009): The cortico-basal ganglia integrative network: the role of the thalamus. Brain
480 research bulletin, 78(2-3), 69-74.

481 Harris GJ, Codori AM, Lewis RF, Schmidt E, Bedi A, Brandt J (1999): Reduced basal ganglia blood flow and
482 volume in pre-symptomatic, gene-tested persons at-risk for Huntington's disease. Brain 122(9): 1667-1678.

483 Kim EY, Johnson HJ (2013): Robust multi-site MR data processing: iterative optimization of bias correction, tissue
484 classification, and registration. Frontiers in neuroinformatics 7: 29.

485 Liu W, Yang J, Burgunder J, Cheng B, Shang H (2016): Diffusion imaging studies of Huntington's disease: A meta-
486 analysis. Parkinsonism & Related Disorders 32: 94-101.

487 Lu W, Johnson H (2010): Introduction to ITK resample in-place image filter. The insight journal 3-6.

488 Lyall AE, Pasternak O, Robinson DG, Newell D, Trampush JW, Gallego JA, et al. (2017): Greater extracellular
489 free-water in first-episode psychosis predicts better neurocognitive functioning. Molecular Psychiatry.

490 Macdonald V, Halliday G (2002): Pyramidal cell loss in motor cortices in Huntington's disease. Neurobiology of
491 disease 10(3): 378-386.

492 Malcolm JG, Shenton ME, Rathi Y (2010): Filtered multitensor tractography. IEEE transactions on medical
493 imaging 29(9): 1664-1675.

494 Matsui JT, Vaidya JG, Johnson HJ, Magnotta VA, Long JD, Mills JA, et al. (2014): Diffusion weighted imaging of
495 prefrontal cortex in prodromal Huntington's disease. Human brain mapping 35(4): 1562-1573.

496 Michailovich O, Rathi Y, Dolui S (2011): Spatially regularized compressed sensing for high angular resolution
497 diffusion imaging. IEEE transactions on medical imaging 30(5): 1100-1115.

498 Niccolini F, Politis M (2014): Neuroimaging in Huntington's disease. World journal of radiology 6(6): 301.

499 Nopoulos P, Magnotta VA, Mikos A, Paulson H, Andreasen NC, Paulsen JS (2007). Morphology of the cerebral
500 cortex in preclinical Huntington's disease. American Journal of Psychiatry 164(9): 1428-1434.

501 O'Donnell LJ, Westin CF (2007): Automatic tractography segmentation using a high-dimensional white matter
502 atlas. IEEE transactions on medical imaging 26(11): 1562-1575.

503 Oguz I, Farzinfar M, Matsui J, Budin F, Liu Z, Gerig, G, et al. (2014): DTIPrep: quality control of diffusion-
504 weighted images. Frontiers in neuroinformatics 8: 4.

505 Panagiotaki E, Schneider T, Siow B, Hall MG, Lythgoe MF, Alexander DC (2012): Compartment models of the
506 diffusion MR signal in brain white matter: a taxonomy and comparison. Neuroimage, 59(3): 2241-2254.

507 Pasternak O, Westin CF, Dahlben B, Bouix S, Kubicki M (2015): The extent of diffusion MRI markers of
508 neuroinflammation and white matter deterioration in chronic schizophrenia. Schizophrenia research 161(1): 113-118.

509 Pasternak O, Sochen N, Gur Y, Intrator N, Assaf Y (2009): Free water elimination and mapping from diffusion MRI.
510 Magnetic Resonance in Medicine 62(3): 717-730.

511 Paulsen JS, Langbehn DR, Stout JC, Aylward E, Ross CA, Nance M, et al. (2008): Detection of Huntington's
512 disease decades before diagnosis: the Predict-HD study. Journal of Neurology, Neurosurgery & Psychiatry 79(8):
513 874-880.

514 Paulsen JS, Long JD, Ross CA, Harrington DL, Erwin CJ, Williams JK, et al. (2014): Prediction of manifest
515 Huntington's disease with clinical and imaging measures: A prospective observational study. Lancet Neurol 13(12):
516 1193–1201.

517 Paulsen JS, Magnotta VA, Mikos AE, Paulson HL, Penziner E, Andreasen NC, et al. (2006): Brain structure in
518 preclinical Huntington's disease. Biological psychiatry 59(1): 57-63.

519 Phillips O, Sanchez-Castaneda C, Elifani F, Maglione V, Di Pardo A, Caltagirone C, et al. (2013): Tractography of
520 the corpus callosum in Huntington's disease. PloS one 8(9): e73280.

521 Phillips O, Squitieri F, Sanchez-Castaneda C, Elifani F, Caltagirone C, Sabatini U, et al. (2014): Deep white matter
522 in Huntington's disease. PloS one 9(10): e109676.

523 Pinherio JC, Bates DM (2004): Mixed-effects models in S and S-PLUS. Statistics and Computing Series.

524 Planetta PJ, Ofori E, Pasternak O, Burciu RG, Shukla P, DeSimone JC, et al. (2016): Free-water imaging in
525 Parkinson's disease and atypical parkinsonism. Brain 139 (Pt 2): 495-508.

526 Poudel GR, Stout JC, Churchyard A, Chua P, Egan GF, Georgiou-Karistianis N (2015): Longitudinal change in
527 white matter microstructure in Huntington's disease: The IMAGE-HD study. Neurobiology of disease 74: 406-412.

528 Poudel GR, Stout JC, Salmon L, Churchyard A, Chua P, Georgiou-Karistianis N, et al. (2014): White matter
529 connectivity reflects clinical and cognitive status in Huntington's disease. Neurobiology of disease 65: 180-187.

530 Rathi Y, Michailovich O, Laun F, Setsompop K, Grant PE, Westin CF (2014) Multi-shell diffusion signal recovery
531 from sparse measurements. Medical image analysis 18(7): 1143-1156.

532 Reddy CP, Rathi Y (2016): Joint Multi-Fiber NODDI Parameter Estimation and Tractography Using the Unscented
533 Information Filter. Frontiers in Neuroscience 10: 166.

534 Reilmann R (2014): Huntington disease: natural history, biomarkers and prospects for therapeutics. Nature reviews
535 Neurology 10: 204-216.

536 Rosas HD, Hevelone ND, Zaleta AK, Greve DN, Salat DH, Fischl B (2005): Regional cortical thinning in
537 preclinical Huntington disease and its relationship to cognition. Neurology 65(5): 745-747.

538 Rosas HD, Tuch DS, Hevelone ND, Zaleta AK, Vangel M, Hersch SM, et al. (2006): Diffusion tensor imaging in
539 presymptomatic and early Huntington's disease: selective white matter pathology and its relationship to clinical
540 measures. Movement Disorders 21(9): 1317-1325.

541 Ross CA, Aylward EH, Wild EJ, Langbehn DR, Long JD, Warner JH, Scahill RI, Leavitt BR, Stout JC, Paulsen JS,

542 Rotenberg D, Pasternak O, Shenton M, Voineskos A (2015): Correction for Extracellular Free Water Eliminates
543 Associations of Fractional Anisotropy with Aging and Neurodegenerative Disease. Biological Psychiatry 77(9):
544 95S-95S.

545 Shaffer JJ, Ghayoor A, Long JD, Kim RE, Lourens S, O'Donnell LJ, et al. (2016): Longitudinal diffusion changes in
546 prodromal and early HD: evidence of white-matter tract deterioration. Human Brain Mapping.

547 Singhal T, Kim CK (2017): Putaminal Hypometabolism Exceeding Caudate Abnormalities on 18F-FDG PET in
548 Huntington Disease. Clinical Nuclear Medicine 42(7): e343-344.

549 Steventon JJ, Trueman RC, Da Ma EY, Bayram-Weston Z, Modat, M, Cardoso J, et al. (2016): Longitudinal in vivo
550 MRI in a Huntington's disease mouse model: Global atrophy in the absence of white matter microstructural
551 damage. Scientific Reports 6.

552 Stoffers D, Sheldon S, Kuperman JM, Goldstein J, Corey-Bloom J, Aron AR (2010): Contrasting gray and white
553 matter changes in preclinical Huntington disease An MRI study. Neurology 74(15): 1208-1216.

554 Tabrizi SJ, Langbehn DR, Leavitt BR, Roos RA, Durr A, Craufurd D, et al. (2009): Biological and clinical
555 manifestations of Huntington's disease in the longitudinal TRACK-HD study: cross-sectional analysis of baseline
556 data. The Lancet Neurology 8(9): 791-801.

557 Tabrizi SJ, Reilmann R, Roos RA, Durr A, Leavitt B, Owen G, et al. (2012): Potential endpoints for clinical trials in
558 premanifest and early Huntington's disease in the TRACK-HD study: analysis of 24 month observational data. The
559 Lancet Neurology 11(1): 42-53.

560 Tabrizi SJ, Scahill RI, Durr A, Roos RA, Leavitt BR, Jones R, et al. (2011): Biological and clinical changes in
561 premanifest and early stage Huntington's disease in the TRACK-HD study: the 12-month longitudinal analysis. The
562 Lancet Neurology 10(1): 31-42.

563 Tabrizi SJ, Scahill RI, Owen G, Durr A, Leavitt BR, Roos RA, et al. (2013): Predictors of phenotypic progression
564 and disease onset in premanifest and early-stage Huntington's disease in the TRACK-HD study: analysis of 36-
565 month observational data. The Lancet Neurology 12: 637-649.

566 Thieben MJ, Duggins AJ, Good CD, Gomes L, Mahant N, Richards F, et al. (2002): The distribution of structural
567 neuropathology in pre-clinical Huntington's disease. Brain 125(8): 1815-1828.

568 Vonsattel JPG, DiFiglia M (1998): Huntington disease. Journal of neuropathology and experimental neurology 57(5):
569 369.

570 Vonsattel JPG, Keller C, del Pilar Amaya M (2008): Neuropathology of Huntington's disease. Handbook of clinical
571 neurology 89: 599-618.

572 Wassermann D, Makris N, Rathi Y, Shenton M, Kikinis R, Kubicki M, Westin CF (2016): The white matter query
573 language: a novel approach for describing human white matter anatomy. Brain Structure and Function 221(9): 4705-
574 4721.

575 Wang Y, Wang Q, Haldar JP, Yeh FC, Xie M, Sun P, Tu TW, Trinkaus K, Klein RS, Cross AH, Song SK (2011):
576 Quantification of increased cellularity during inflammatory demyelination. Brain, 134(12): 3590-3601.

577 Zhang Y, Long JD, Mills JA, Warner JH, Lu W, Paulsen JS (2011): Indexing disease progression at study entry with
578 individuals at-risk for Huntington disease. American Journal of Medical Genetics Part B: Neuropsychiatric Genetics
579 156(7): 751-763.

580 Zielonka D, Marinus J, Roos R, Michele G, Donato SD, Putter H, Marcinkowski J, Squitieri F, Bentivoglio AR,
581 Landwehrmeyer GB (2013): The influence of gender on phenotype and disease progression in patients with
582 Huntington's disease. Parkinsonism & related disorders 19(2): 192-197.

583 Zhang H, Schneider T, Wheeler-Kingshott CA, Alexander DC (2012): NODDI: practical in vivo neurite orientation
584 dispersion and density imaging of the human brain. Neuroimage, 61(4): 1000-1016.

Table 1 Demographic and clinical information of the PREDICT-HD sample used in the experiments. *The corresponding parameters were not available for some subjects. SD: standard deviation.

	Normal Control (N = 88, total scans: 219)	Huntington's Disease (N = 243, total scans: 611)
# Male	35 (39.77%)	75 (30.86%)
# Female	53 (60.23%)	168 (69.14%)
Age (Mean ± SD, [Min, Max])	48.58 ± 12.61, [23.19, 87.73]	45.62 ± 12.48, [18.84, 82.72]
Maximum Education Years	15.08 ± 2.56, [9, 20]	14.82± 2.47, [9, 20] (3 unavailable*)
CAG Repeats	20.68 ± 3.80, [15, 35]	42.10 ± 2.70, [37, 58]
Total Motor Scores	3.08 ± 4.15, [0, 30] (10 unavailable*)	9.11 ± 11.21, [0, 77] (8 unavailable*)
Diagnostic Confidence Level	0.58 ± 0.66, [0, 3] (10 unavailable*)	1.32 ± 1.29, [0, 4] (8 unavailable*)

Table 2 Summary of the representative MRI parameters used by each manufacturer. Diffusion-weighted imaging (DWI) data was acquired with 32 – 237 directions; TR: repetition time; TE: echo time; TI: inversion time.

Mode	Manufacturer	TR (ms)	TE (ms)	TI (ms)	Thickness (mm)	Acquisition Matrix	Bandwidth (Hz/pixel)	Flip Angle
T1	GE	6.5	2.8	400	1	256, 256, 216	244.1	12
	Philips	7.7	3.5		1.1	220, 218, 164	241	8
	Siemens	2,300	2.87	900	1.1	256, 256, 240	238	10
T2	GE	3,000	82.5		1.4	288, 288, 160	244.1	90
	Philips	2,500	183.6		1.1	220, 218, 164	583	90
	Siemens	4,800	430		1.4	256, 250, 160	592	90
DWI	GE	17,000	87.2		2.4	128, 128	1,953.12	90
	Philips	9,679	92		2	128, 128	1,566.02	90
	Siemens	12,000	92		2	128, 128	1,565	90

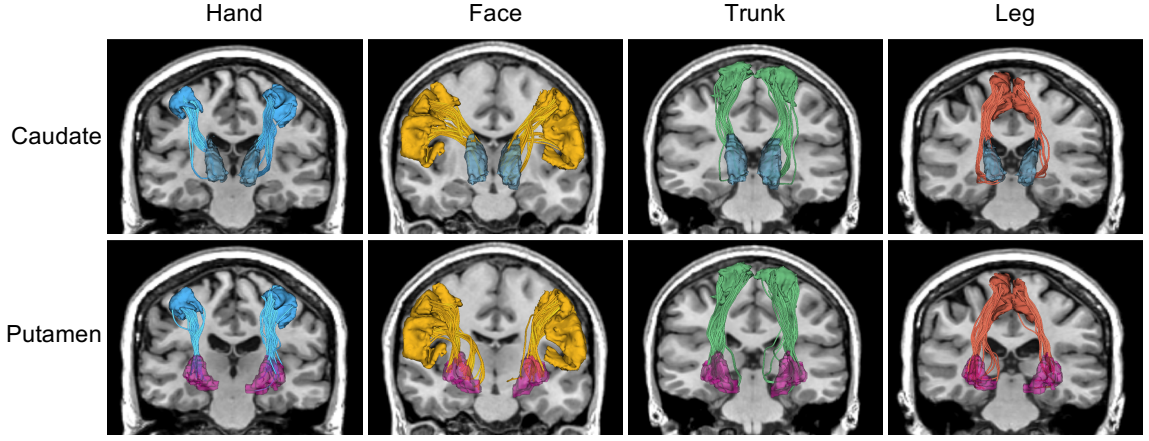
Hand
Face
Trunk
Leg
Caudate
Putamen

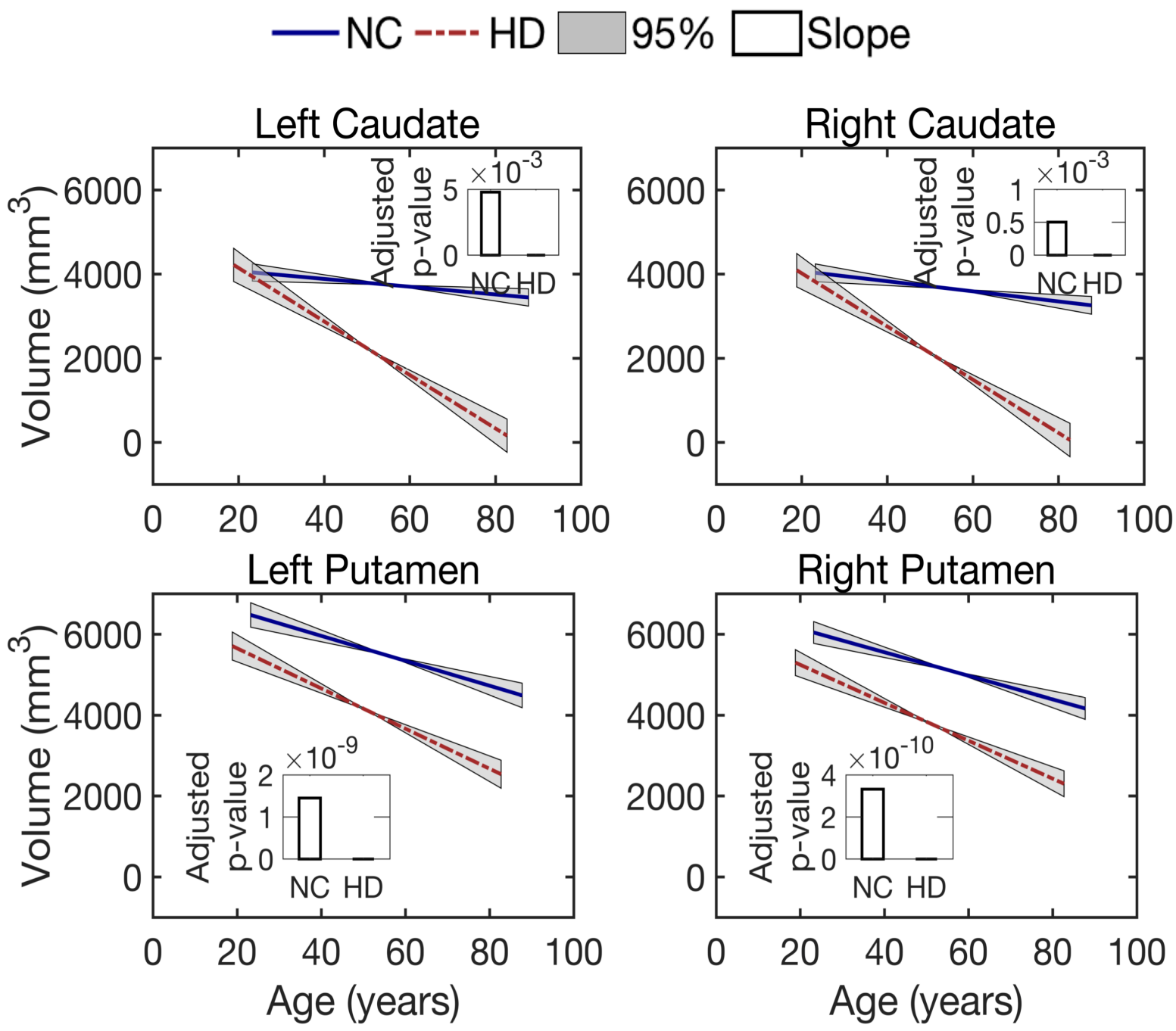
NC
HD
95%
Slope
Left Caudate
Right Caudate
Left Putamen
Right Putamen
Volume (mm3)
Age (years)
Adjusted p-value
×10-3
×10-9
×10-10
NC HD
0
20
40
60
80
100
2000
4000
6000

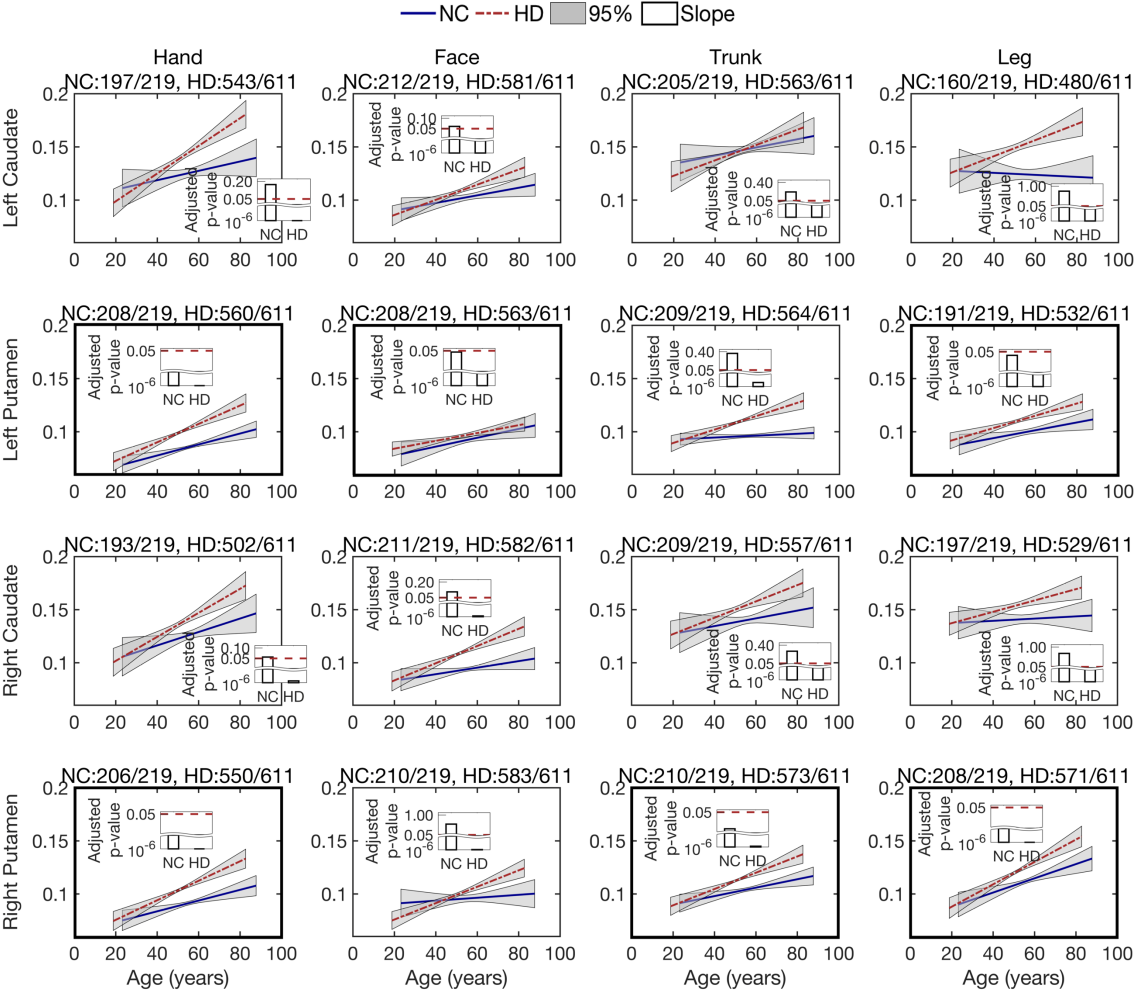
NC
HD
95%
Slope
Hand
Face
Trunk
Leg
Left Caudate
Left Putamen
Right Caudate
Right Putamen
NC:197/219, HD:543/611
NC:212/219, HD:581/611
NC:205/219, HD:563/611
NC:160/219, HD:480/611
NC:208/219, HD:560/611
NC:208/219, HD:563/611
NC:209/219, HD:564/611
NC:191/219, HD:532/611
NC:193/219, HD:502/611
NC:211/219, HD:582/611
NC:209/219, HD:557/611
NC:197/219, HD:529/611
NC:206/219, HD:550/611
NC:210/219, HD:583/611
NC:210/219, HD:573/611
NC:208/219, HD:571/611
Adjusted p-value
NC HD
Age (years)

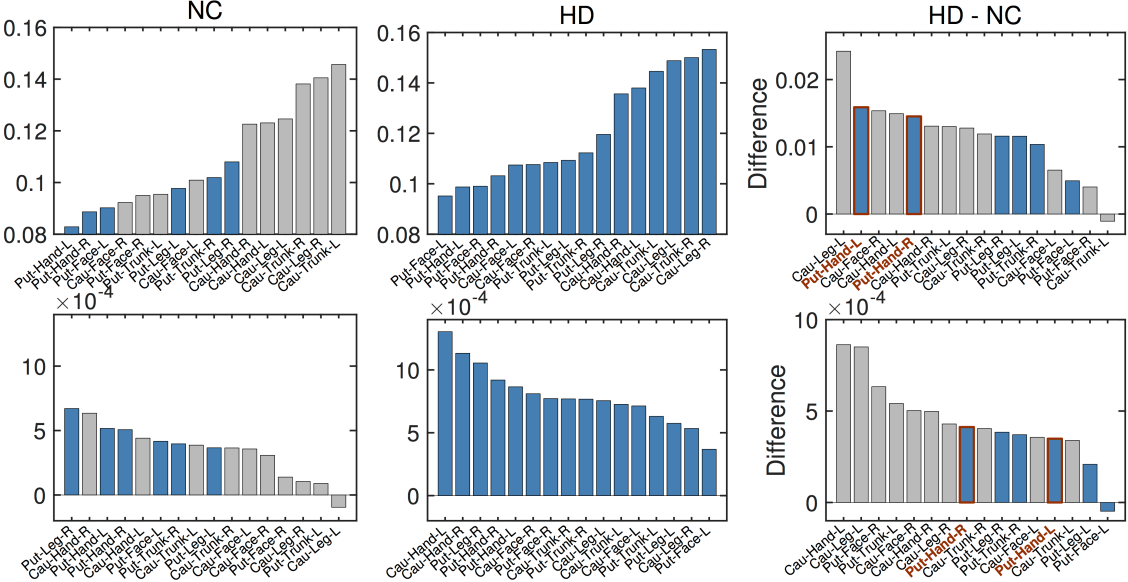
NC
HD
HD - NC
Difference
0.16
0.14
0.12
0.1
0.08
0.02
0.01
0
Put-Hand-L
Put-Hand-R
Put-Face-L
Cau-Face-R
Put-Trunk-L
Put-Leg-L
Cau-Face-L
Put-Trunk-R
Put-Leg-R
Cau-Hand-R
Cau-Hand-L
Cau-Leg-L
Cau-Trunk-R
Cau-Leg-R
Cau-Trunk-L
Cau-Leg-L
×10^-4
10
5
0
Put-Leg-R
Cau-Hand-L
Cau-Hand-R
Put-Hand-L
Put-Hand-R
Cau-Face-L
Put-Face-L
Put-Trunk-L
Cau-Trunk-L
Put-Leg-L
Cau-Face-R
Put-Face-R
Cau-Leg-R
Put-Trunk-R
Put-Leg-L
Cau-Hand-L
Cau-Hand-R
Put-Hand-L
Put-Hand-R
Cau-Face-L
Cau-Face-R
Put-Face-R
Put-Face-L
Cau-Trunk-R
Cau-Trunk-L
Put-Leg-R
Put-Trunk-R
Put-Leg-L
Cau-Leg-L
Cau-Leg-R
Cau-Hand-L
Cau-Leg-L
Put-Face-R
Cau-Face-R
Cau-Hand-R
Put-Trunk-R
Cau-Trunk-L
Put-Hand-R
Put-Leg-R
Cau-Face-L
Put-Hand-L
Cau-Trunk-R
Put-Leg-L
Put-Face-L

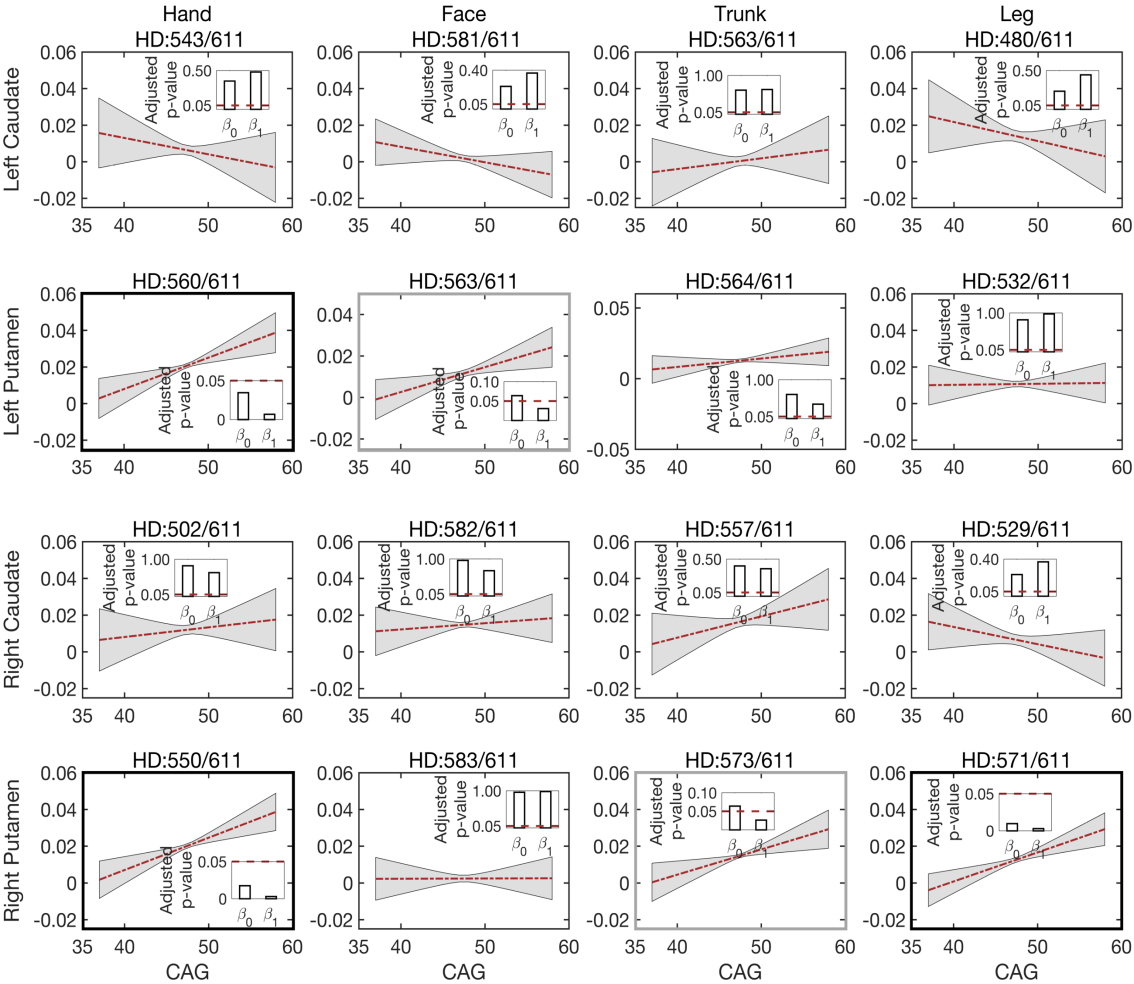
Hand
Face
Trunk
Leg
Left Caudate
Left Putamen
Right Caudate
Right Putamen
HD:543/611
HD:581/611
HD:563/611
HD:480/611
HD:560/611
HD:563/611
HD:564/611
HD:532/611
HD:502/611
HD:582/611
HD:557/611
HD:529/611
HD:550/611
HD:583/611
HD:573/611
HD:571/611
Adjusted p-value
CAG

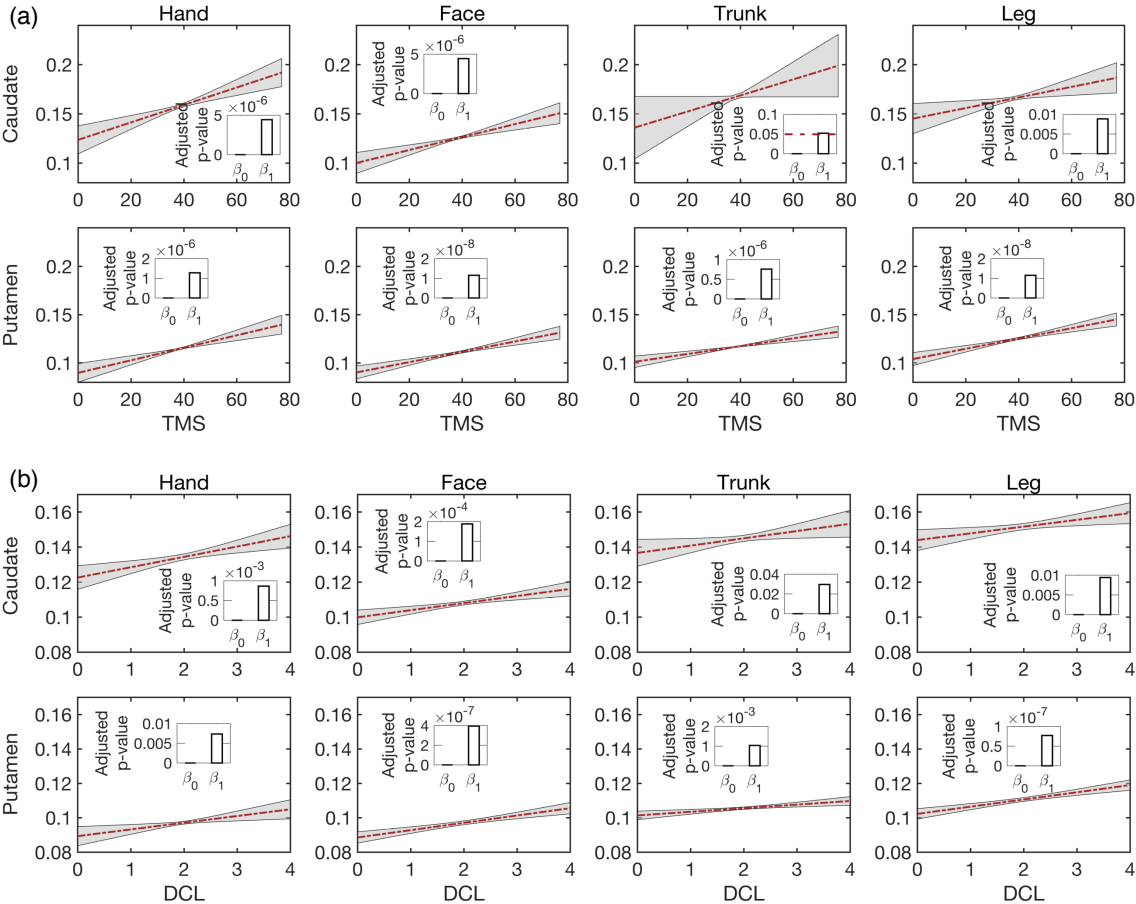
(a)
Hand
Face
Trunk
Leg
Caudate
Putamen
TMS
Adjusted p-value
β_0 β_1
(b)
DCL

Supplementary material

Table 1 The slope, t-statistic, estimated degrees of freedom (DF), and associated FDR-corrected p-values for correlation between caudate and putamen volume loss and age (cf. Fig. 2). All correlations are significant at a significance level of 0.05.

	Normal Control				Huntington's Disease			
	Slope	t-Stat	DF	p-Value	Slope	t-Stat	DF	p-Value
Left Caudate	-9.2347	-2.8497	216	$4.7991e^{-3}$	-63.6013	-10.075	603	$1.4442e^{-21}$
Right Caudate	-12.0076	-3.6132	214	$5.0257e^{-4}$	-63.2369	-9.9663	607	$1.8083e^{-21}$
Left Putamen	-30.8260	-6.4565	211	$1.4495e^{-9}$	-49.6062	-8.9647	603	$3.8796e^{-18}$
Right Putamen	-29.0864	-6.8354	215	$3.3251e^{-10}$	-46.8855	-9.1738	602	$9.6031e^{-19}$

Table 2 The slope, t-statistic, estimated degrees of freedom (DF), and associated FDR-corrected p-values for correlation between isotropic volume fraction and age (cf. Fig. 3). *In these regions, normal control or Huntington's disease groups show significant changes in free water fraction at a significance level of 0.05.

		Normal Control				Huntington's Disease			
		Slope (10^{-3})	t-Stat	DF	p-Values	Slope (10^{-3})	t-Stat	DF	p-Values
	Hand	0.4410	1.6148	194	0.1728	1.3038	6.4163	539	$1.3002e^{-9*}$
Left	Face	0.3571	2.1778	210	0.0611	0.7133	4.8499	575	$2.3160e^{-6*}$
Caudate	Trunk	0.3868	1.4445	203	0.2184	0.7259	3.2555	561	0.0013^{*}
	Leg	-0.0953	-0.2988	157	0.7655	0.7553	3.7125	476	0.0003^{*}
	Hand	0.5166	4.3121	202	0.0004^{*}	0.8653	6.4029	555	$1.3002e^{-9*}$
Left	Face	0.4167	2.3924	205	0.0470^{*}	0.3687	3.5611	558	0.0005^{*}
Putamen	Trunk	0.0893	1.0394	201	0.3691	0.6306	5.3025	558	$2.9310e^{-7*}$
	Leg	0.3662	2.5095	182	0.0415^{*}	0.5750	4.8706	524	$2.3160e^{-6*}$

	Hand	0.6344	2.2620	188	0.0568	1.1323	5.4890	496	$1.2921e^{-7*}$
Right	Face	0.3077	1.8964	206	0.1054	0.8103	5.6908	573	$5.3852e^{-8*}$
Caudate	Trunk	0.3650	1.2484	204	0.2844	0.7693	3.7406	555	0.0003^{*}
	Leg	0.1047	0.4490	194	0.6975	0.5340	3.1855	526	0.0015^{*}
	Hand	0.5069	3.4185	200	0.0041^{*}	0.9193	6.5131	546	$1.3002e^{-9*}$
Right	Face	0.1388	0.6830	205	0.5662	0.7718	5.9120	578	$1.8502e^{-8*}$
Putamen	Trunk	0.3968	3.0431	206	0.0106^{*}	0.7675	5.6617	561	$5.4746e^{-8*}$
	Leg	0.6707	3.7390	205	0.0019^{*}	1.0549	6.8896	561	$2.4118e^{-10*}$

Table 3 The intercept and slope with their t-statistic, estimated degrees of freedom (DF), and associated FDR-corrected p-values for correlation between isotropic volume fraction and the genetic load, CAG (cf. Fig. 5). *****indicates significant correlations (FDR corrected p-value < 0.05).

		β_0				β_1			
		Intercept	t-Stat	DF	P-Values	Slope (10^{-3})	t-Stat	DF	p-Values
	Hand	0.0489	1.2676	538	0.3653	-0.8964	-0.9734	538	0.4812
Left	Face	0.0420	1.6034	575	0.2334	-0.8452	-1.3806	575	0.3704
Caudate	Trunk	-0.0275	-0.7290	561	0.6217	0.5862	0.6585	561	0.6383
	Leg	0.06341	1.5716	472	0.2334	-1.0428	-1.0868	472	0.4443
	Hand	-0.0605	-2.7329	556	0.0345^{*}	1.7114	3.2387	556	0.0068^{*}
Left	Face	-0.0454	-2.3334	558	0.0639	1.2007	2.5994	558	0.0307^{*}
Putamen	Trunk	-0.0155	-0.7814	558	0.6217	0. 5938	1.2595	558	0.3704
	Leg	0.0079	0.3586	524	0.8229	0. 0575	0.1094	524	0.9738
	Hand	-0.0130	-0.3780	496	0.8229	0. 5266	0.6459	496	0.6383
Right	Face	-0.0014	-0.0503	574	0.9599	0.3392	0.5299	574	0.6816
Caudate	Trunk	-0.0387	-1.1404	555	0.4074	1.1603	1.4335	555	0.3704
	Leg	0.0512	1.6662	526	0.2334	0.9404	-1.2840	526	0.3704

	Hand	-0.0633	-3.0764	546	0.0176*	1.7583	3.5795	546	0.0030*
Right	Face	0.0017	0.0739	579	0.9599	0.0138	0.0247	579	0.9803
Putamen	Trunk	-0.0505	-2.3971	562	0.0639	1.3746	2.7283	562	0.0263*
	Leg	-0.0624	-3.4471	561	0.0097	1.5809	3.7022	561	0.0030*

Table 4 The slope, t-statistic, estimated degrees of freedom (DF), and associated FDR-corrected p-values for correlation of isotropic volume fraction and clinical scores (total motor scores and diagnostic confidence level, cf. Fig. 6). Except for the connection from trunk to the caudate (colored in red), isotropic volume fractions in other regions are significantly correlated with total motor scores /diagnostic confidence level.

		Total Motor Scores				Diagnostic Confidence Level			
		Slope (10^{-3})	t-Stat	DF	p-Values	Slope	t-Stat	DF	p-Values
Caudate	Hand	0.8886	4.7418	461	$4.4355e^{-6}$	0.0059	3.5451	460	0.0009
	Face	0.6563	4.6976	552	$4.4355e^{-6}$	0.0041	4.0057	552	0.0002
	Trunk	0.8182	1.9485	521	**0.0519**	0.0041	2.1821	521	0.0296
	Leg	0.5393	2.6763	432	0.0088	0.0038	2.6551	432	0.0094
Putamen	Hand	0.6479	5.0405	527	$1.2785e^{-6}$	0.0039	2.7872	526	0.0073
	Face	0.5353	6.1561	537	$1.1525e^{-8}$	0.0043	5.4032	539	$3.9358e^{-7}$
	Trunk	0.4044	5.1996	539	$7.5747e^{-7}$	0.0021	3.4316	537	0.0010
	Leg	0.5330	6.0492	493	$1.1528e^{-8}$	0.0042	5.8373	495	$7.6851e^{-8}$